

Beyond-mean-field studies of Wigner crystal transitions in various interacting two-dimensional systems

Zhongqing Guo¹ and Jianpeng Liu^{1, 2, 3, *}

¹*School of Physical Science and Technology, ShanghaiTech University, Shanghai 201210, China*

²*ShanghaiTech Laboratory for Topological Physics,*

ShanghaiTech University, Shanghai 201210, China

³*Liaoning Academy of Materials, Shenyang 110167, China*

In this work, we theoretically study Wigner crystal (WC) transitions in various interacting two-dimensional electron gas (2DEG) models, including both conventional 2DEG model and “ n -order” Dirac fermion models with energy-momentum dispersion $E_{\mathbf{k}} \sim k^n$, with n being positive integer. A general “ $GW+RPA$ ” framework to treat single-particle spectra and ground-state energies in 2D systems has been developed. Within such a framework, we first calculate the single-particle excitation spectra of a conventional 2DEG system with GW approximation for both Wigner-crystal state and Fermi-liquid (FL) state, in which the frequency dependent dielectric function is treated using a multiple-plasma-pole approach. Then, the correlation energy with random phase approximation (RPA) is further calculated based on the GW single-particle spectra. By comparing the total energies of WC and FL states, our $GW+RPA$ approach gives a critical Wigner-Seitz radius $r_s^* \sim 19.2$ for the WC transition in conventional 2DEG system. We then apply such $GW+RPA$ method to single-flavor n -order Dirac fermion models, unveiling the unique single-particle excitation spectra in these models. We further find that charge fluctuations would de-stabilize the presumable WC states, including both topologically trivial and nontrivial WC states. Our method can be readily applied to other interacting 2D systems described by continuum models such as moiré superlattices.

Introduction – When the carrier density is sufficiently low, interacting two-dimensional electron gas (2DEG) system would undergo a transition from gapless Fermi liquid (FL) state to charge-gapped Wigner crystal (WC) state [1–11]. The latter spontaneously break spatial translational symmetry, forming a quantum electronic lattice with the lattice constant uniquely defined by the carrier density. Such WC transition problem in 2DEG is notoriously difficult to treat theoretically. The only reliable numerical approach is quantum Monte Carlo (QMC) method, which gives a critical Wigner-Seitz radius $r_s^* \sim 31$ [5, 12], quantitatively consistent with the result obtained from transport measurements [3]. However, QMC is numerically demanding, and usually suffers from sign problem. Thus, its applicability to other interacting 2D systems would be limited. Other numerical methods based on mean-field theory, such as Hartree-Fock [4], would highly overestimate the tendency of forming a WC state due to the negligence of correlation energy induced by charge fluctuations. Therefore, it would be helpful to develop a reliable and efficient many-body numerical method that is generally applicable to various 2D systems.

To this end, we develop a general “ $GW+RPA$ ” framework to treat single-particle spectra and ground-state energies of interacting two-dimensional (2D) systems. Taking conventional 2DEG as an example, we first calculate the ground-state energy and single-particle spectra of the system under Hartree-Fock approximation, where two trial wavefunctions have been used: one is the WC state that spontaneously breaks translational symmetry, and the other is the FL state. Then, we calculate the

frequency dependent GW single-particle self energy [13–16], which gives more accurate descriptions to the single-particle excitation spectra for both WC state and FL state. Particularly, the frequency dependent dielectric function in the GW self energy is treated using a multiple plasma pole approach [17, 18]. Since Hartree-Fock calculations neglect correlation energy, we further calculate correlation energy with random phase approximation (RPA) based on the GW single-particle spectra [19, 20]. By comparing the total energies (including kinetic, Hartree, exchange, and correlation energies) of FL and WC states, our $GW+RPA$ approach gives a critical Wigner-Seitz radius $r_s^* \sim 19.2$ for the WC transition in conventional 2DEG system, which is much better than the result from Hartree-Fock ($r_s^* \sim 2$) or Hartree-Fock+RPA ($r_s^* \sim 4$) calculations. This indicates that such $GW+RPA$ framework can be generally applied to other interacting 2D systems.

Besides conventional 2DEG, various two-dimensional Dirac-fermion models may also be realized in condensed matter systems. It is well known that massless Dirac fermions with linear energy-band dispersion can emerge in monolayer graphene [21, 22]. Moreover, even “high-order” Dirac fermions with energy-momentum dispersion $E_{\mathbf{k}} \sim k^n$ may approximately describe the low-energy single-particle excitations in n -layer graphene with rhombohedral stacking [23, 24]. This motivates us to theoretically study the WC transitions in a broad class of charge-doped n -order Dirac fermion models. Several fundamental questions need to be answered in such n -order Dirac fermion models with charge doping. First, is there any WC transition happening when these Dirac fermion mod-

els are charge-doped? Second, since the Dirac fermions would acquire non-vanishing Berry curvature once the Dirac point is gapped, would there be any topological properties associated with the presumable WC state? Lastly, what are the characteristics of the single-particle spectra in these n -order Dirac fermion models? To answer these questions, we apply the GW +RPA method to charge-doped interacting n -order Dirac fermion models. We find that Hartree-Fock calculations would predict two competing WC states as the ground state of n -order Dirac fermions at low carrier densities: one has zero Chern number forming a spontaneous triangular lattice, and the other has Chern number 1 forming a honeycomb lattice. However, it turns out that charge fluctuations would de-stabilize both types of presumable WC states due to the less correlation energy gain compared to the FL state. Moreover, plasmaron-like (or plasma-polaron-like) excitation features are seen in the single-particle spectra of these Dirac-fermion models.

GW+RPA method – We consider the long-range Coulomb interaction Hamiltonian which applies to both 2DEG and n -order Dirac fermion systems, expressed as:

$$H_C = \frac{1}{2N_s} \sum_{\lambda, \lambda'} \sum_{\mathbf{k}, \mathbf{k}', \mathbf{q}} V(\mathbf{q}) \hat{c}_{\mathbf{k}+\mathbf{q}, \lambda}^\dagger \hat{c}_{\mathbf{k}'-\mathbf{q}, \lambda'}^\dagger \hat{c}_{\mathbf{k}', \lambda'} \hat{c}_{\mathbf{k}, \lambda}, \quad (1)$$

where N_s is the total number of unit cells (of presumable WC state) in the system, \mathbf{k} and \mathbf{q} represent the wave vectors expanded around some low-energy valleys, and $\lambda \equiv (\mu, \alpha, \sigma)$ is a composite index denoting the (possible) valley, (possible) sublattice, and spin degrees of freedom. The Coulomb interaction is in the double-gate screened form, given by $V(\mathbf{q}) = e^2 \tanh(|\mathbf{q}|d_s)/(2\Omega_0 \epsilon_r \epsilon_0 |\mathbf{q}|)$, where d_s represents the screening length, Ω_0 is the area of a unit cell, ϵ_r is the relative dielectric constant, and ϵ_0 is the vacuum permittivity.

Initially, we solve this interaction using the self-consistent unrestricted Hartree-Fock (HF) approximation in a plane-wave basis set. At this stage, the total energy includes contributions from the kinetic, Hartree, and exchange energies. However, HF neglects electron correlation effects, and thus tends to favor symmetry-breaking states such as WC state. To improve upon this, we introduce the correlation energy through random phase approximation (RPA). RPA captures collective electron-hole excitations, counterbalancing the HF bias toward symmetry-breaking state. The RPA correlation energy is expressed as [19, 20, 25, 26]:

$$E_c^{\text{RPA}} = \frac{1}{4\pi} \int_{-\infty}^{\infty} d\omega \text{Tr} [\ln (1 - V\chi^0(i\omega)) + V\chi^0(i\omega)] \quad (2)$$

where V is the Coulomb potential and χ^0 represents the non-interacting charge polarizability.

Since the accuracy of the RPA correlation energy relies on the accuracy of single-particle excitation spectra, we further employ the GW approximation [13–16, 27, 28] to

improve the HF band structures. In the GW approximation, the electron self-energy Σ_c is calculated as:

$$\Sigma_c(\mathbf{r}, \mathbf{r}', \omega) = \frac{i}{2\pi} \int d\nu e^{i\nu\delta^+} G_0(\mathbf{r}, \mathbf{r}', \omega + \nu) W_{\text{RPA}}(\mathbf{r}', \mathbf{r}, \nu) \quad (3)$$

where G_0 is the HF Green's function and W_{RPA} is the dynamically screened Coulomb interaction:

$$W_{\text{RPA}}(\mathbf{r}, \mathbf{r}', \omega) = \int d\mathbf{r}'' [\epsilon_{\text{RPA}}^{-1}(\mathbf{r}, \mathbf{r}'', \omega) - \delta(\mathbf{r}, \mathbf{r}'')] V(\mathbf{r}'', \mathbf{r}') \quad (4)$$

where the static part has been subtracted as it is already taken into account in the HF calculations.

In this formalism, the inverse dielectric function $\epsilon_{\text{RPA}}^{-1}$ plays a critical role in capturing the frequency-dependent screening of the Coulomb interaction. The quasiparticle (QP) energies are then corrected through the GW self-energy, expressed as:

$$\varepsilon_{n\mathbf{k}}^{\text{QP}} = \varepsilon_{n\mathbf{k}}^{\text{HF}} + Z_{n\mathbf{k}} \text{Re} \Sigma_c(\mathbf{k}, \varepsilon_{n\mathbf{k}}^{\text{HF}})_{nn} \quad (5)$$

where $Z_{n\mathbf{k}} = [1 - \text{Re}(\partial \Sigma_c(\mathbf{k}, \omega)_{nn}/\partial \omega)_{\omega=\varepsilon_{n\mathbf{k}}^{\text{HF}}}]^{-1}$ is the QP weight, accounting for interaction renormalization effects of QPs in the FL state. In order to handle the frequency dependence of the dielectric function efficiently, we employ the multiple plasmon pole approximation (MPA) [17, 18, 29], which allows for a more precise and efficient treatment of the screening effects. Further details on the HF approximation, GW approximation, and MPA are provided in the Supplementary Information [29]. These methods allow us to obtain a more accurate and balanced description of both exchange and correlation effects. As will be presented in the following, both ground-state energies and single-particle spectra obtained using such GW +RPA method are significantly improved compared with those obtained from HF or HF+RPA calculations.

Conventional 2DEG – 2DEG system with the kinetic energy expressed as

$$H_{\text{2DEG}}^0(\mathbf{k}) = \frac{\hbar^2 \mathbf{k}^2}{2m^*}, \quad (6)$$

serves as a fundamental platform for investigating many-body physics, including the Wigner crystallization and its transition to FL state. The key parameter controlling the WC transition is the dimensionless Wigner-Seitz radius $r_s = g_\nu g_s m^*/(\sqrt{\pi n} \epsilon_r m_0 a_B)$ (g_ν and g_s are the valley and spin degeneracies, respectively, n is the electron density, ϵ_r is the relative dielectric constant, m^* is the effective mass, m_0 is the electron mass, and a_B is the Bohr radius), which measures the average inter-electron separation and characterizes the balance between kinetic and interaction energies. Using the GW +RPA framework introduced earlier, we calculate the single-particle excitation spectra in a triangular electronic lattice with

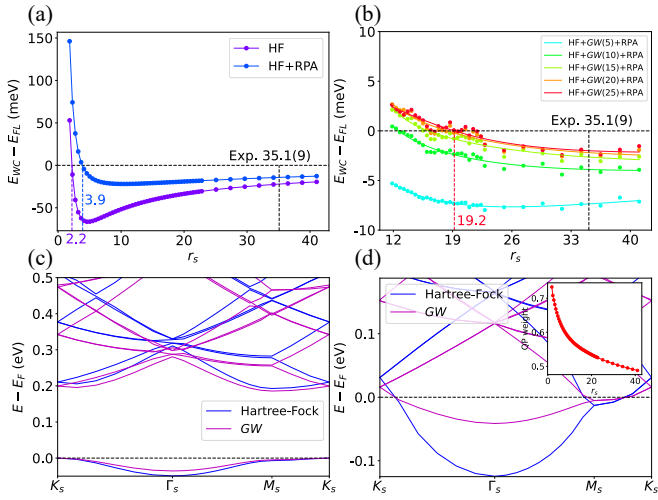


FIG. 1. (a) Condensation energy as a function of r_s based on HF and HF+RPA calculations. (b) Condensation energy as a function of r_s based on HF+GW+RPA calculations with increasing number of HF bands corrected by GW correction. (b) Band structure of fully spin-polarized WC state at $r_s = 11.4$. (c) Band structure of spin-degenerate FL state at $r_s = 11.4$. The inset shows the QP weight for the FL state as a function of r_s .

one electron per unit cell for fully spin polarized state and two electrons per unit cell for spin unpolarized state.

In Fig. 1(a), we show the condensation energy, $E_{\text{cond.}} = E_{WC} - E_{FL}$ as a function of r_s , where E_{WC} (E_{FL}) denotes total energy of WC (FL) state. The results from HF calculations, as marked by the purple line, significantly overestimate the stability of the WC state by neglecting electron correlation effects. In the HF approximation, the transition to the WC phase occurs at a smaller $r_s \sim 2.2$, suggesting an much earlier transition than the experimental value 35.1(9) [3]. The blue line in Fig. 1(a) shows the results after incorporating RPA correlation energy, which captures collective charge-fluctuation effects and partly corrects HF's bias toward WC state. Including the RPA correlation energy shifts the WC transition to larger values of $r_s \sim 3.9$ with lower electron density, highlighting the critical role of correlations in stabilizing the FL state.

We further refined these calculations using the GW +RPA method, as shown in Fig. 1(b). The inclusion of additional GW corrections to the HF bands (labeled by “ GW (5-25)” with 5-25 denoting the number of HF bands corrected by GW self energy) progressively shifts the critical r_s to larger values, ultimately converging around $r_s^* \sim 19.2$ (data fitting is described in Supplementary Information [5, 12, 29]), a value that matches experimental results for 2DEG systems much closer than those without GW corrections. This demonstrates that the combination of RPA and GW corrections better captures the delicate balance between exchange and correla-

tion effects, providing a more accurate prediction of the WC transition.

Fig. 1(c) shows the QP band structure of a fully spin-polarized WC state at $r_s = 11.4$. After including electron interactions, a gap opens at the Brillouin zone (of the Wigner lattice) boundary due to strong Coulomb interactions. When the GW correction is applied, charge fluctuations screen part of the Coulomb interaction, reducing both the HF gap and the bandwidth. Fig. 1(d) presents the spin-degenerate FL state at the same $r_s = 11.4$. After applying the GW correction, the bandwidth significantly decreases leading to larger effective mass due to correlation effects. The reduction in both the gap and bandwidth due to the GW correction results in a large absolute value of the RPA correlation energy, which further corrects the HF exchange energy and reduces HF's bias toward the WC state. Additionally, from the GW calculation, we obtain the QP weight for the FL state, as shown in the inset of Fig. 1(d). As r_s increases, the QP weight gradually decreases, implying more important correlation effects and the eventual breakdown of the Fermi liquid description. These results suggest the GW +RPA method can faithfully describe the WC transition problem in conventional 2DEG system, thus can be readily extended to other interacting 2D systems with long-range Coulomb interactions.

Dirac fermion models – After being benchmarked in conventional 2DEG, we continue to apply our GW +RPA framework to high-order Dirac-fermion models to explore whether WC transitions would occur when these systems are charge-doped. This is built on our motivation to understand how electron-electron interactions influence phase transitions in rhombohedral multilayer graphene systems. The corresponding low-energy non-interacting Hamiltonian is approximately described by n -order Dirac fermion models for the n -layer graphene system, expressed as:

$$H_{\mu,n}^0(\mathbf{k}) = -t_{\perp} \begin{pmatrix} \Delta & (\nu_{\mu}^{\dagger})^n \\ (\nu_{\mu})^n & -\Delta \end{pmatrix} \quad (7)$$

where $\nu_{\mu} = \hbar v_F(\mu k_x + ik_y)/t_{\perp}$, v_F is the Fermi velocity, and t_{\perp} is the interlayer hopping amplitude, $\mu = \mp$ denotes K/K' valley of graphene. Δ denotes the Dirac-fermion mass which physically originates from vertical electric field applied to rhombohedral multilayer graphene. Unless specified otherwise, we set $\hbar v_F = 5.25 \text{ eV} \cdot \text{\AA}$, $t_{\perp} = 0.34 \text{ eV}$, and $\Delta = 0.1 \text{ eV}$ throughout the paper.

In Fig. 2(a), we first present the energy spectrum of Dirac fermions in monolayer graphene after HF calculations with 10% electron doping with respect to charge neutrality, incorporating the GW self-energy correction. The main HF bands are clearly visible, along with surrounding satellite features. These satellites arise from electron-plasmon interactions, representing plasmaron or

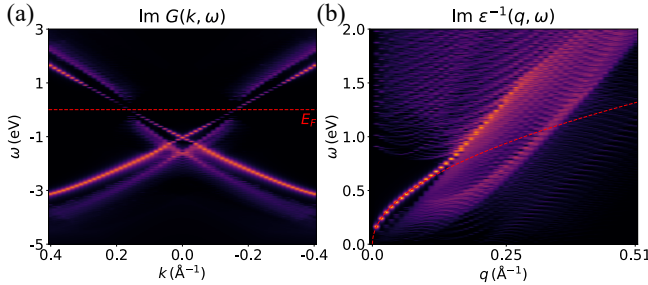


FIG. 2. (a) Energy spectrum of Dirac fermions in monolayer graphene with 10% electron doping. (b) Collective excitation spectrum.

plasmon-polaron states, consistent with previous theoretical and experimental reports [30–32].

We continue to study n -order Dirac fermions which approximately describes the low-energy band dispersions in n -layer rhombohedral graphene ($n = 2, 3, 4, 5$, and 6) [23]. Here we assume that at low carrier densities, the ground state is fully spin-valley polarized as observed in experiments [33], so that flavor (spin/valley) fluctuations are expected to make less important contributions to self energy and correlation energy compared to charge fluctuations within a single flavor. This justifies our $GW + RPA$ approach in treating charge-doped single-flavor Dirac-fermion models.

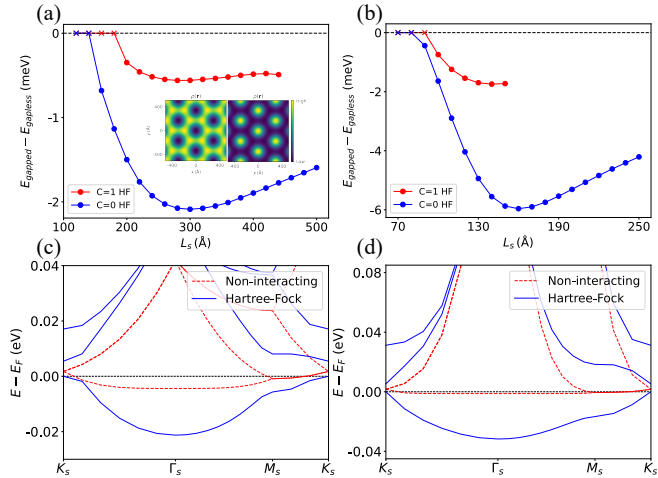


FIG. 3. (a) Condensation energies as a function of L_s for the $n = 2$ Dirac-fermion model based on HF calculations. The insets show real-space electron distributions for two distinct WC states. (b) Condensation energies as a function of L_s for the $n = 5$ system based on HF calculations. (c) Chern-number-1 band structure of $n = 2$ system at $L_s = 200 \text{\AA}$. (d) Chern-number-1 band structure for $n = 5$ system at $L_s = 100 \text{\AA}$.

Fig.3(a) shows the WC condensation energy as a function of lattice constant L_s for the $n = 2$ model calculated only in HF approximation. Two distinct WC states are observed: the Chern-number-0 WC state (blue line)

emerges for $L_s \geq 120 \text{\AA}$, while the Chern-number-1 state (red line) exists in the range $L_s = 200 \sim 440 \text{\AA}$. The Chern-number-0 WC state consistently has lower energy, indicating that the topologically trivial ground state is energetically favorable under HF approximation. The insets in Fig.3(a) display the real-space electron distributions: the left inset shows that of the Chern-number-1 WC state, where electrons form a honeycomb lattice [34], and the right inset shows the Chern-number-0 WC state, where electrons form a triangular lattice. Similarly, Fig. 3(b) presents the results for the $n = 5$ model, where the behavior is similar to that of the $n = 2$ case. The Chern-number-0 WC state (blue line) exists for $L_s \geq 90 \text{\AA}$, while the Chern-number-1 WC state (red line) emerges in the range $L_s = 100 \sim 150 \text{\AA}$. Again, the topologically trivial WC state always has lower HF energy. Figs. 3(c) and 3(d) depict the band structures for $n = 2$ system at $L_s = 200 \text{\AA}$ and for $n = 5$ system at $L_s = 100 \text{\AA}$, respectively. The red dashed lines represent the non-interacting bands, while the blue solid lines show the HF band structures in the Chern-number-1 WC states. We see that strong interaction effects would open up a gap at the corresponding Brillouin zone corner, and in the meanwhile the bandwidth is enhanced by interactions in the HF framework due to exchange-hole effects.

It is worth noting that the Berry curvature of the non-interacting conduction band of the n -order Dirac-fermion model can be calculated analytically: $\Omega(\mathbf{k}, n) = \gamma^2 n^2 \Delta k^{2n-2} / (2(\gamma^2 k^{2n} + \Delta^2)^{3/2}$, where $\gamma = (-1/t_{\perp})^{n-1} v_F^n$. The Berry curvature is peaked at the wavevector k_{peak} : $k_{\text{peak}} = \left(\frac{n-1}{n+2}\right)^{\frac{1}{2n}} \Delta^{\frac{1}{n}} t_{\perp}^{\frac{n-1}{n}} / v_F$. As n increases, k_{peak} shifts toward larger value. Actually, our HF calculations indicate that whenever the Fermi wavevector k_F coincides with k_{peak} , the system would undergo WC transition at a critical lattice constant L_s^* , with the distance between Γ_s and K_s in its first Brillouin zone given by $4\pi/(3L_s^*) \sim k_F \sim k_{\text{peak}}$.

Figs.4(a) and 4(b) illustrate the effects of including RPA correlation energy (blue) based on HF calculations, and based on GW -corrected QPs (red). It can be seen that neither the Chern-number 0 nor the Chern-number 1 WC states remain as the ground state any more. Instead, the FL state becomes the ground state for all L_s . The inclusion of correlation effects not only counteracts the bias of exchange energy towards WC states but also leads to their destabilization. Fig.4(c) shows the single-particle spectrum of the FL state for the pentalayer system ($n = 5$ model) at $L_s = 100$, which reveals plasmon satellites similar to those observed in Fig.2(a). A detailed discussion of these features is provided in the Supplementary Information [29]. The inset in Fig. 4(c) shows how the QP weight decreases with the increase of L_s , suggesting stronger correlation effects at lower density. Fig. 4(d) presents the GW quasiparticle band structure for the pentalayer system ($n = 5$) in the WC state. The

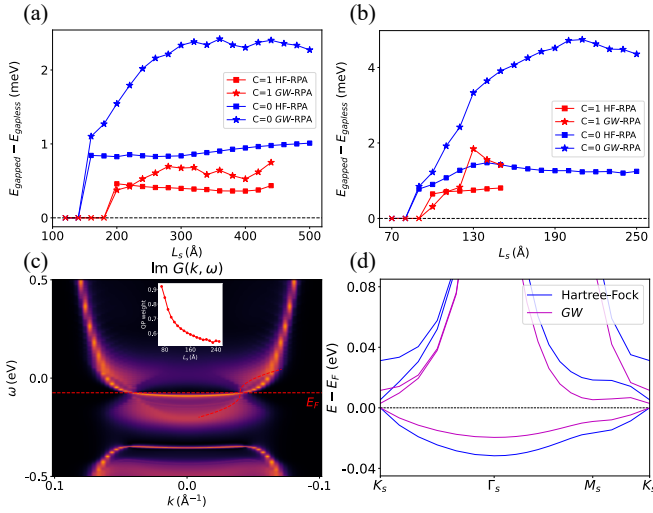


FIG. 4. (a) Condensation energy as a function of L_s for the $n = 2$ Dirac-fermion model based on HF+RPA and HF+GW+RPA calculations. (b) Condensation energy as a function of L_s for the $n = 5$ Dirac-fermion model based on HF+RPA and HF+GW+RPA calculations. (c) Single-particle spectrum of the FL state for the $n = 5$ model at $L_s = 100$ Å. The inset shows the QP weight for the FL state as a function of L_s . (d) GW quasiparticle band structures of the Chern-number-1 WC state for the $n = 5$ Dirac-fermion model at $L_s = 100$ Å.

GW correction reduces both the gap and the bandwidth due to dynamic screening of Coulomb interactions.

Conclusion – To summarize, we have developed a comprehensive “*GW+RPA*” framework to study the WC transitions in both conventional 2DEG system and various n -order Dirac-fermion models. In conventional 2DEG systems, we found that the WC transition occurs at a critical Wigner-Seitz radius $r_s^* \sim 19.2$, which closely matches experimental observations and is significantly improved compared with the results from HF and HF+RPA calculations. When applying this framework to charge-doped n -order Dirac fermion models, we have investigated the properties of the potential WC states and explored their stabilities under charge fluctuations. HF calculations predicted competing WC states, one with Chern number 0 forming a triangular lattice, and the other with Chern number 1 forming a honeycomb lattice. However, after accounting for correlation effects through RPA and *GW+RPA* corrections, charge fluctuations tend to destabilize both WC states. Our theoretical framework can be readily applied to other interacting 2D systems described by continuum models such as moiré superlattices.

We thank Xinguo Ren for valuable discussions. This work is supported by the National Natural Science Foundation of China (grant No. 12174257) and National Key R & D program of China (grant No. 2020YFA0309601).

* liujp@shanghaitech.edu.cn

- [1] E. Wigner, Phys. Rev. **46**, 1002 (1934).
- [2] E. Y. Andrei, G. Deville, D. C. Glattli, F. I. B. Williams, E. Paris, and B. Etienne, Phys. Rev. Lett. **60**, 2765 (1988).
- [3] J. Yoon, C. C. Li, D. Shahar, D. C. Tsui, and M. Shayegan, Phys. Rev. Lett. **82**, 1744 (1999).
- [4] J. R. Trail, M. D. Towler, and R. J. Needs, Phys. Rev. B **68**, 045107 (2003).
- [5] N. D. Drummond and R. J. Needs, Phys. Rev. Lett. **102**, 126402 (2009).
- [6] B. Padhi, C. Setty, and P. W. Phillips, Nano Lett. **18**, 6175 (2018).
- [7] E. C. Regan, D. Wang, C. Jin, M. I. B. Utama, B. Gao, X. Wei, S. Zhao, W. Zhao, Z. Zhang, K. Yumigeta, et al., Nature **579**, 359 (2020).
- [8] E. C. Regan, D. Wang, C. Jin, M. I. Bakti Utama, B. Gao, X. Wei, S. Zhao, W. Zhao, Z. Zhang, K. Yumigeta, M. Blei, J. D. Carlström, K. Watanabe, T. Taniguchi, S. Tongay, M. Crommie, A. Zettl, and F. Wang, Nature **579**, 359 (2020).
- [9] H. Li, S. Li, E. C. Regan, D. Wang, W. Zhao, S. Kahn, K. Yumigeta, M. Blei, T. Taniguchi, K. Watanabe, S. Tongay, A. Zettl, M. F. Crommie, and F. Wang, Nature **597**, 650 (2021).
- [10] Y. Zhou, J. Sung, E. Brutschea, I. Esterlis, Y. Wang, G. Scuri, R. J. Gelly, H. Heo, T. Taniguchi, K. Watanabe, et al., Nature **595**, 48 (2021).
- [11] Y.-C. Tsui, M. He, Y. Hu, E. Lake, T. Wang, K. Watanabe, T. Taniguchi, M. P. Zaletel, and A. Yazdani, Nature **628**, 287 (2024).
- [12] F. Rapisarda and G. Senatore, Australian journal of physics **49**, 161 (1996).
- [13] L. Hedin, Phys. Rev. **139**, A796 (1965).
- [14] F. Aryasetiawan and O. Gunnarsson, Reports on Progress in Physics **61**, 237 (1998).
- [15] L. Reining, WIREs Computational Molecular Science **8**, e1344 (2018).
- [16] D. Golze, M. Dvorak, and P. Rinke, Frontiers in chemistry **7**, 377 (2019).
- [17] D. A. Leon, C. Cardoso, T. Chiarotti, D. Varsano, E. Molinari, and A. Ferretti, Phys. Rev. B **104**, 115157 (2021).
- [18] D. A. Leon, A. Ferretti, D. Varsano, E. Molinari, and C. Cardoso, Phys. Rev. B **107**, 155130 (2023).
- [19] D. Bohm and D. Pines, Phys. Rev. **92**, 609 (1953).
- [20] M. Gell-Mann and K. A. Brueckner, Phys. Rev. **106**, 364 (1957).
- [21] K. S. Novoselov, A. K. Geim, S. V. Morozov, D.-e. Jiang, Y. Zhang, S. V. Dubonos, I. V. Grigorieva, and A. A. Firsov, Science **306**, 666 (2004).
- [22] A. H. Castro Neto, F. Guinea, N. M. R. Peres, K. S. Novoselov, and A. K. Geim, Rev. Mod. Phys. **81**, 109 (2009).
- [23] H. Min and A. H. MacDonald, Progress of Theoretical Physics Supplement **176**, 227 (2008).
- [24] J. Liu, Z. Ma, J. Gao, and X. Dai, Phys. Rev. X **9**, 031021 (2019).
- [25] A. L. Fetter and J. D. Walecka, Quantum theory of many-particle systems (Courier Corporation, 2012).

- [26] X. Ren, P. Rinke, C. Joas, and M. Scheffler, *Journal of Materials Science* **47**, 7447 (2012).
- [27] M. S. Hybertsen and S. G. Louie, *Phys. Rev. B* **34**, 5390 (1986).
- [28] G. Onida, L. Reining, and A. Rubio, *Rev. Mod. Phys.* **74**, 601 (2002).
- [29] See Supplemental Information (including Refs. [5, 12–20, 23–28, 30–32, 35–40]) for: (a) detailed formalism for the Hartree-Fock calculations, (b) details of the *GW* calculations, (c) detailed formalism multiple plasmon pole approximation, (d) details of the random phase approximation for correlation energy, (e) data fitting for critical Wigner-Seitz radius r_s^* in 2DEG, and (f) more results about n -order Dirac fermion models for $n=2, 3, 4, 5$, and 6.
- [30] A. Bostwick, F. Speck, T. Seyller, K. Horn, M. Polini, R. Asgari, A. H. MacDonald, and E. Rotenberg, *Science* **328**, 999 (2010).
- [31] P. E. Trevisanutto, C. Giorgetti, L. Reining, M. Ladisa, and V. Olevano, *Phys. Rev. Lett.* **101**, 226405 (2008).
- [32] H. Zhang, S. Wang, E. Wang, X. Lu, Q. Li, C. Bao, K. Deng, H. Zhang, W. Yao, G. Chen, A. V. Fedorov, J. D. Denlinger, K. Watanabe, T. Taniguchi, G. Zhang, and S. Zhou, *npj Quantum Materials* **6**, 83 (2021).
- [33] T. Han, Z. Lu, G. Scuri, J. Sung, J. Wang, T. Han, K. Watanabe, T. Taniguchi, H. Park, and L. Ju, *Nature Nanotechnology* , 1 (2023).
- [34] Y. Zeng, D. Guerci, V. Crépel, A. J. Millis, and J. Cano, *Phys. Rev. Lett.* **132**, 236601 (2024).
- [35] X. Lu, S. Zhang, Y. Wang, X. Gao, K. Yang, Z. Guo, Y. Gao, Y. Ye, Z. Han, and J. Liu, *Nature Communications* **14**, 5550 (2023).
- [36] S. B. Zhang, D. Tománek, M. L. Cohen, S. G. Louie, and M. S. Hybertsen, *Phys. Rev. B* **40**, 3162 (1989).
- [37] R. W. Godby and R. J. Needs, *Phys. Rev. Lett.* **62**, 1169 (1989).
- [38] W. von der Linden and P. Horsch, *Phys. Rev. B* **37**, 8351 (1988).
- [39] G. E. Engel and B. Farid, *Phys. Rev. B* **47**, 15931 (1993).
- [40] R. Côté and A. H. MacDonald, *Phys. Rev. B* **44**, 8759 (1991).

Supplemental Material for “Beyond-mean-field studies of Wigner crystal transitions in various interacting two-dimensional systems”

I. HARTREE-FOCK APPROXIMATION FOR TWO-DIMENSIONAL SYSTEMS

The Hartree-Fock (HF) approximation is a standard method to treat interacting electronic systems. Our HF framework is implemented in the plane-wave basis, where an electron annihilation operator $\hat{c}_\lambda(\mathbf{k})$ with flavor index λ and wavevector \mathbf{k} (expanded around some low-energy valley), can be re-written as:

$$\hat{c}_{\lambda, \mathbf{G}}(\tilde{\mathbf{k}}) \equiv \hat{c}_\lambda(\mathbf{k}), \quad (1)$$

where $\lambda \equiv (\mu, \alpha, \sigma)$ is a composite flavor index denoting the (possible) valley, (possible) sublattice, and spin degrees of freedom. Wavevector \mathbf{k} is expanded around some low-energy valley, and is further decomposed into a reciprocal vector \mathbf{G} and a wavevector $\tilde{\mathbf{k}}$ within the Brillouin zone of the corresponding lattice. The non-interacting Hamiltonian of the system can be generally expressed as:

$$H^0 = \sum_{\lambda, \lambda', \tilde{\mathbf{k}}, \mathbf{G}} H_{\lambda, \lambda'}^0(\tilde{\mathbf{k}} + \mathbf{G}) \hat{c}_{\lambda, \mathbf{G}}^\dagger(\tilde{\mathbf{k}}) \hat{c}_{\lambda', \mathbf{G}}(\tilde{\mathbf{k}}). \quad (2)$$

For the conventional two-dimensional electron gas (2DEG) system, the kinetic energy is simply given by:

$$H_{\text{2DEG}}^0(\mathbf{k}) = \frac{\hbar^2 \mathbf{k}^2}{2m^*}, \quad (3)$$

where m^* is the effective mass of the electrons, $\mathbf{k} = \tilde{\mathbf{k}} + \mathbf{G}$. For n -order Dirac fermion models, which describe n -layer graphene system, the kinetic energy term is [23, 24]:

$$H_{\mu, n}^0(\mathbf{k}) = -t_\perp \begin{pmatrix} \Delta & (\nu_\mu^\dagger)^n \\ (\nu_\mu)^n & -\Delta \end{pmatrix}, \quad (4)$$

where $\nu_\mu = \hbar v_F(\mu k_x + ik_y)/t_\perp$, v_F is the Fermi velocity, and t_\perp is the interlayer hopping amplitude, $\mu = \mp$ denotes K/K' valley of graphene. Δ denotes the Dirac-fermion mass which physically originates from vertical electric field applied to rhombohedral multilayer graphene. Unless specified otherwise, we set $\hbar v_F = 5.25 \text{ eV} \cdot \text{\AA}$, $t_\perp = 0.34 \text{ eV}$, and $\Delta = 0.1 \text{ eV}$ throughout the paper.

In this work, we consider the Coulomb interaction only in the intravalley form, neglecting the intervalley interactions, which is usually exponentially smaller than the intravalley one. This assumption simplifies the interaction Hamiltonian and is justified because intravalley interactions are generally the dominant contributions at low energies. The interaction Hamiltonian within this approximation is written as [35]:

$$H_C^{\text{intra}} = \frac{1}{2N_s} \sum_{\lambda, \lambda'} \sum_{\tilde{\mathbf{k}}, \tilde{\mathbf{k}'}, \mathbf{q}} \sum_{\mathbf{G}, \mathbf{G}', \mathbf{Q}} V(\tilde{\mathbf{q}} + \mathbf{Q}) \hat{c}_{\lambda, \mathbf{G} + \mathbf{Q}}^\dagger(\tilde{\mathbf{k}} + \tilde{\mathbf{q}}) \hat{c}_{\lambda', \mathbf{G}' - \mathbf{Q}}^\dagger(\tilde{\mathbf{k}}' - \tilde{\mathbf{q}}) \hat{c}_{\lambda', \mathbf{G}'}(\tilde{\mathbf{k}}') \hat{c}_{\lambda, \mathbf{G}}(\tilde{\mathbf{k}}). \quad (5)$$

Here, N_s denotes the total number of unit cells (of the presumable Wigner crystal state) in the system. Assuming that the ground state always preserves lattice translational symmetry, the expectation value of the density operator is expressed as:

$$\langle \hat{c}_{\lambda, \mathbf{G} + \mathbf{Q}}^\dagger(\tilde{\mathbf{k}} + \tilde{\mathbf{q}}) \hat{c}_{\lambda', \mathbf{G}}(\tilde{\mathbf{k}}') \rangle = \langle \hat{c}_{\mu, \alpha, \mathbf{G} + \mathbf{Q}}^\dagger(\tilde{\mathbf{k}}') \hat{c}_{\mu', \alpha', \mathbf{G}}(\tilde{\mathbf{k}}') \rangle \delta_{\tilde{\mathbf{k}} + \tilde{\mathbf{q}}, \tilde{\mathbf{k}'}} \delta_{\sigma, \sigma'}. \quad (6)$$

Then, the Hartree term reads:

$$V^H = \frac{1}{N_s} \sum_{\tilde{\mathbf{k}}, \tilde{\mathbf{k}'}} \sum_{\lambda, \lambda'} \sum_{\mathbf{G}, \mathbf{G}', \mathbf{Q}} V(\mathbf{Q}) \langle \hat{c}_{\lambda', \mathbf{G}' - \mathbf{Q}}^\dagger(\tilde{\mathbf{k}}') \hat{c}_{\lambda', \mathbf{G}'}(\tilde{\mathbf{k}}') \rangle \hat{c}_{\lambda, \mathbf{G} + \mathbf{Q}}^\dagger(\tilde{\mathbf{k}}) \hat{c}_{\lambda, \mathbf{G}}(\tilde{\mathbf{k}}), \quad (7)$$

and the Fock term reads:

$$\begin{aligned} V_F &= -\frac{1}{N_s} \sum_{\tilde{\mathbf{k}}, \tilde{\mathbf{k}'}} \sum_{\lambda, \lambda'} \sum_{\mathbf{G}, \mathbf{G}', \mathbf{Q}} V(\tilde{\mathbf{k}}' - \tilde{\mathbf{k}} + \mathbf{Q}) \langle \hat{c}_{\lambda, \mathbf{G} + \mathbf{Q}}^\dagger(\tilde{\mathbf{k}}') \hat{c}_{\lambda', \mathbf{G}'}(\tilde{\mathbf{k}}') \rangle \hat{c}_{\lambda', \mathbf{G}' - \mathbf{Q}}^\dagger(\tilde{\mathbf{k}}) \hat{c}_{\lambda, \mathbf{G}}(\tilde{\mathbf{k}}) \\ &= -\frac{1}{N_s} \sum_{\tilde{\mathbf{k}}, \tilde{\mathbf{k}'}} \sum_{\lambda, \lambda'} \sum_{\mathbf{G}, \mathbf{G}', \mathbf{Q}} V(\tilde{\mathbf{k}}' - \tilde{\mathbf{k}} + \mathbf{G}' - \mathbf{G} + \mathbf{Q}) \langle \hat{c}_{\lambda, \mathbf{G}' + \mathbf{Q}}^\dagger(\tilde{\mathbf{k}}') \hat{c}_{\lambda', \mathbf{G}'}(\tilde{\mathbf{k}}') \rangle \hat{c}_{\lambda', \mathbf{G} - \mathbf{Q}}^\dagger(\tilde{\mathbf{k}}) \hat{c}_{\lambda, \mathbf{G}}(\tilde{\mathbf{k}}). \end{aligned} \quad (8)$$

In these equations, $\langle \dots \rangle$ represents the expectation value of the operator in the many-body ground state $|\Psi\rangle^0$, which is assumed to be a Slater-determinant state in the HF framework. To achieve a self-consistent solution, the HF calculations are carried out iteratively for different superlattice constants L_s . The background dielectric constant is set to $\epsilon_r = 4$. To initialize the HF self-consistent loop, the expectation values of density operators $\langle \hat{c}_{\lambda, \mathbf{G}' - \mathbf{Q}}^\dagger(\mathbf{k}') \hat{c}_{\lambda, \mathbf{G}'}(\mathbf{k}') \rangle$ are chosen to reflect either a spontaneous charge order with non-zero Fourier component at $\mathbf{Q} \neq \mathbf{0}$, corresponding to the Wigner crystal (WC) state; or it is set to zero, corresponding to the Fermi liquid (FL) state. We compare the total energy $E_{\text{total}} = E_{\text{kinetic}} + E_{\text{HF}}$ of these two types of states to determine the genuine ground state. Here E_{kinetic} is the kinetic energy, and E_{HF} is the HF energy including both Hartree and exchange energies. In our calculations, a 9×9 mesh of reciprocal lattice points (centered at the Γ point) has been used for the 2DEG system, while a 3×3 mesh is used for n -order Dirac fermion systems. The mini Brillouin zone (of the presumable WC state) is sampled by an 18×18 \mathbf{k} -mesh. For verification, calculations with a 13×13 reciprocal-lattice mesh (for 2DEG) have been performed for 2DEG, showing that the results obtained using 7×7 mesh are already converged. The results for the n -order Dirac fermion systems are benchmarked with 5×5 and 7×7 reciprocal-lattice mesh, which also yield quantitatively consistent results, as shown in Supplementary Figure 1.

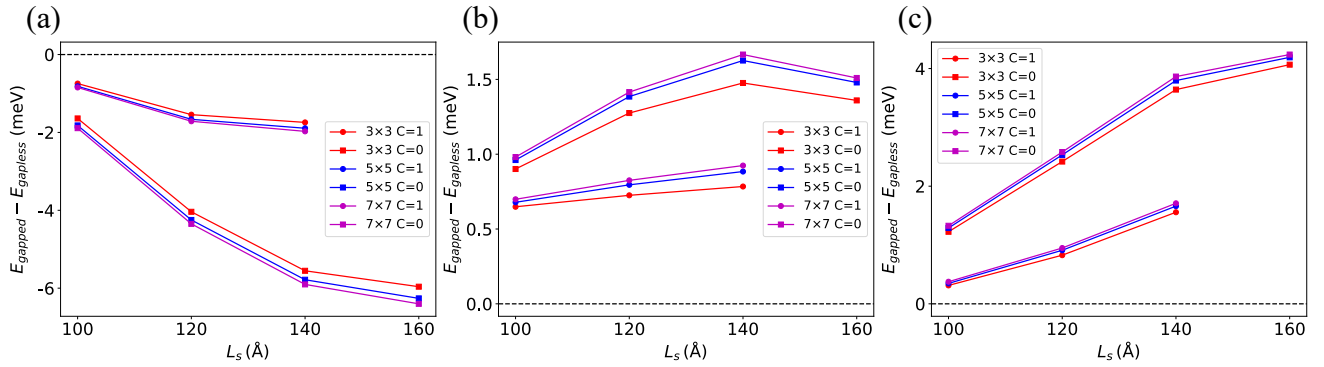


FIG. 1. Wigner-crystal condensation energy of $n = 5$ Dirac fermion system as a function of the corresponding superlattice constant L_s : (a) results from Hartree-Fock calculations; (b) results from Hartree-Fock+RPA calculations; (c) results from GW +RPA calculations. The red, blue and purple lines represent results calculated using 3×3 , 5×5 , and 7×7 reciprocal meshes, respectively. The solid circles and squares represent the results for the Chern-number-1 and Chern-number-0 Wigner crystal states, respectively.

II.GW APPROXIMATION FOR TWO-DIMENSIONAL SYSTEMS

The GW approximation provides a framework for incorporating electron-electron interactions beyond the mean-field HF theory [13–16, 27, 28]. It improves the description of quasiparticle (QP) energies and the single-particle energy spectrum by including the effects of dynamic screening. The key equations in the GW formalism are known as Hedin’s equations, which describe a set of self-consistent equations of self-energy Σ , Green’s function G , vertex function Γ , polarization propagator P , and screened Coulomb interaction W . For simplicity, here we use Arabic number as a short-hand notation for spatial (\mathbf{r}) and temporal (t) coordinate, e.g., $1 \equiv (\mathbf{r}_1, t_1)$. Then, with such short-hand notations, Hedin’s equations are given by:

$$\Sigma(12) = i \int d3 G(13)W(14)\Gamma(342), \quad (9)$$

$$G(12) = G_0(12) + \int d3 G_0(13)\Sigma(34)G(42), \quad (10)$$

$$\Gamma(123) = \delta(12)\delta(13) + \int d4 d5 \frac{\delta\Sigma(12)}{\delta G(45)} G(46)G(75)\Gamma(673), \quad (11)$$

$$P(12) = -i \int d3 d4 G(13)G(42)\Gamma(342), \quad (12)$$

$$W(12) = V(12) + \int d3 V(13) P(34) W(42). \quad (13)$$

These equations form the basis of many-body perturbation theory, linking the Green's function, self-energy, and screened interaction in a self-consistent framework. To apply the GW approximation, we assume a simple form of vertex function, $\Gamma(123) = \delta(12)\delta(13)$, which leads to the "bare vertex" approximation:

$$\Gamma(123) = \delta(12)\delta(13). \quad (14)$$

Under this approximation, the self-energy simplifies to:

$$\Sigma(12) = iG(12)W(12). \quad (15)$$

Similarly, the polarization reduces to:

$$P(12) = -iG(12)G(21). \quad (16)$$

To describe the screened Coulomb interaction W in terms of the dielectric function ϵ , we express V as:

$$V(12) = \int d3 \epsilon(13) W(32). \quad (17)$$

The dielectric function ϵ can be formulated as:

$$\epsilon(12) = \delta(12) - \int d3 V(13) P(32). \quad (18)$$

We continue to perform a Fourier transform from time domain to frequency domain to handle the time-dependent components. Now we go back to the usual notations where \mathbf{r} (\mathbf{r}') denote real-space coordinate, and ω denote frequency. The non-interacting Green's function G_0 is given by:

$$G_0(\mathbf{r}, \mathbf{r}', \omega) = \sum_{n\tilde{\mathbf{k}}} \frac{\psi_{n\tilde{\mathbf{k}}}(\mathbf{r}) \psi_{n\tilde{\mathbf{k}}}^*(\mathbf{r}')}{\omega - \varepsilon_{n\tilde{\mathbf{k}}} + i\delta \text{sgn}(\varepsilon_{n\tilde{\mathbf{k}}} - \varepsilon_F)}, \quad (19)$$

where $\psi_{n\tilde{\mathbf{k}}}$ are the HF single-particle wave functions, $\varepsilon_{n\tilde{\mathbf{k}}}$ are the HF eigenvalues, and ε_F is the Fermi energy. The non-interacting charge polarizability χ^0 , which characterizes the linear response of the system to external perturbative potentials, is given by:

$$\chi^0(\mathbf{r}, \mathbf{r}', \nu) = -i \int \frac{d\omega}{2\pi} e^{i\omega\delta^+} G_0(\mathbf{r}, \mathbf{r}', \omega + \nu) G_0(\mathbf{r}', \mathbf{r}, \omega). \quad (20)$$

Using χ^0 , the dielectric function within the Random Phase Approximation (RPA) is expressed as:

$$\epsilon_{\text{RPA}}(\mathbf{r}, \mathbf{r}', \omega) = \delta(\mathbf{r}, \mathbf{r}') - \int d\mathbf{r}'' V(\mathbf{r}, \mathbf{r}'') \chi^0(\mathbf{r}'', \mathbf{r}', \omega). \quad (21)$$

The screened Coulomb interaction within RPA is:

$$W_{\text{RPA}}(\mathbf{r}, \mathbf{r}', \omega) = \int d\mathbf{r}'' [\epsilon_{\text{RPA}}^{-1}(\mathbf{r}, \mathbf{r}'', \omega) - \delta(\mathbf{r}, \mathbf{r}'')] V(\mathbf{r}'', \mathbf{r}'), \quad (22)$$

where the static part has been subtracted as it is already taken into account in the HF calculations. The correlation part of the self-energy, Σ_c , which accounts for electron correlation effects beyond HF, is then computed using:

$$\Sigma_c(\mathbf{r}, \mathbf{r}', \omega) = \frac{i}{2\pi} \int d\nu e^{i\nu\delta^+} G_0(\mathbf{r}, \mathbf{r}', \omega + \nu) W_{\text{RPA}}(\mathbf{r}', \mathbf{r}, \nu), \quad (23)$$

where G_0 is the HF Green's function and W_{RPA} is the dynamically screened Coulomb interaction.

Then, we perform a Fourier transform from real space to reciprocal space. The matrix elements of the non-interacting charge polarizability in reciprocal space are:

$$\begin{aligned} \chi_{\mathbf{Q}\mathbf{Q}'}^0(\tilde{\mathbf{q}}, \nu) = & \frac{1}{N\Omega_0} \sum_{n', n, \tilde{\mathbf{k}}} \left[\sum_{\lambda, \mathbf{G}} C_{\lambda\mathbf{G} + \mathbf{Q}, n'\tilde{\mathbf{k}} + \tilde{\mathbf{q}}}^* C_{\lambda\mathbf{G}, n\tilde{\mathbf{k}}} \right]^* \left[\sum_{\lambda', \mathbf{G}'} C_{\lambda'\mathbf{G}' + \mathbf{Q}', n'\tilde{\mathbf{k}} + \tilde{\mathbf{q}}}^* C_{\lambda'\mathbf{G}', n\tilde{\mathbf{k}}} \right] \\ & \times \left[\frac{\theta(\varepsilon_{n'\tilde{\mathbf{k}} + \tilde{\mathbf{q}}} - \varepsilon_F) \theta(\varepsilon_F - \varepsilon_{n\tilde{\mathbf{k}}})}{\nu - \varepsilon_{n'\tilde{\mathbf{k}} + \tilde{\mathbf{q}}} + \varepsilon_{n\tilde{\mathbf{k}}} + i\delta} - \frac{\theta(\varepsilon_F - \varepsilon_{n'\tilde{\mathbf{k}} + \tilde{\mathbf{q}}}) \theta(\varepsilon_{n\tilde{\mathbf{k}}} - \varepsilon_F)}{\nu - \varepsilon_{n'\tilde{\mathbf{k}} + \tilde{\mathbf{q}}} + \varepsilon_{n\tilde{\mathbf{k}}} - i\delta} \right], \end{aligned}$$

where $C_{\lambda\mathbf{G},n\tilde{\mathbf{k}}}$ are the expansion coefficients of the single-particle states in the plane-wave basis, and \mathbf{G} , \mathbf{G}' , \mathbf{Q} , and \mathbf{Q}' denote reciprocal vectors. The matrix form of the RPA dielectric function in reciprocal space is expressed as:

$$\epsilon_{\mathbf{QQ}'}^{\text{RPA}}(\tilde{\mathbf{q}}, \omega) = \delta_{\mathbf{QQ}'} - V(\tilde{\mathbf{q}} + \mathbf{Q})\chi_{\mathbf{QQ}'}^0(\tilde{\mathbf{q}}, \omega), \quad (24)$$

and the screened Coulomb interaction in reciprocal space is given by:

$$W_{\mathbf{QQ}'}^{\text{RPA}}(\tilde{\mathbf{q}}, \omega) = \left[\epsilon_{\mathbf{QQ}'}^{-1, \text{RPA}}(\tilde{\mathbf{q}}, \omega) - \delta_{\mathbf{QQ}'} \right] V(\tilde{\mathbf{q}} + \mathbf{Q}'). \quad (25)$$

The correlation self-energy in reciprocal space can be expressed as:

$$\begin{aligned} \Sigma_c(\tilde{\mathbf{k}}, \omega)_{nn} = & \frac{i}{N\Omega_0} \sum_{m, \tilde{\mathbf{q}}} \sum_{\mathbf{G}, \mathbf{G}'} \left[\sum_{\lambda, \mathbf{Q}} C_{\lambda\mathbf{G}+\mathbf{Q}, m\tilde{\mathbf{k}}+\tilde{\mathbf{q}}}^* C_{\lambda\mathbf{Q}, n\tilde{\mathbf{k}}} \right]^* \left[\sum_{\lambda', \mathbf{Q}'} C_{\lambda'\mathbf{G}'+\mathbf{Q}', m\tilde{\mathbf{k}}+\tilde{\mathbf{q}}}^* C_{\lambda'\mathbf{Q}', n\tilde{\mathbf{k}}} \right] \\ & \times V(\tilde{\mathbf{q}} + \mathbf{G}) \int \frac{d\nu}{2\pi} e^{i\nu\eta} \frac{\left[\epsilon_{\mathbf{G}'\mathbf{G}}^{-1, \text{RPA}}(\tilde{\mathbf{q}}, \nu) - \delta_{\mathbf{GG}'} \right]}{\omega + \nu - \varepsilon_{m\tilde{\mathbf{k}}+\tilde{\mathbf{q}}} + i\delta \text{sgn}(\varepsilon_{m\tilde{\mathbf{k}}+\tilde{\mathbf{q}}} - \varepsilon_F)}. \end{aligned}$$

In this formalism, the inverse dielectric function $\epsilon_{\text{RPA}}^{-1}$ plays a critical role in capturing the frequency-dependent screening of the Coulomb interaction. The QP energies are then corrected through the GW self-energy, expressed as:

$$\varepsilon_{n\tilde{\mathbf{k}}}^{\text{QP}} = \varepsilon_{n\tilde{\mathbf{k}}}^{\text{HF}} + Z_{n\tilde{\mathbf{k}}} \text{Re} \Sigma_c(\tilde{\mathbf{k}}, \varepsilon_{n\tilde{\mathbf{k}}}^{\text{HF}})_{nn}, \quad (26)$$

where $Z_{n\tilde{\mathbf{k}}}$ is the QP weight, accounting for interaction renormalization effects of QPs:

$$Z_{n\tilde{\mathbf{k}}} = \left[1 - \text{Re} \left(\frac{\partial \Sigma_c(\tilde{\mathbf{k}}, \omega)_{nn}}{\partial \omega} \right)_{\omega=\varepsilon_{n\tilde{\mathbf{k}}}^{\text{HF}}} \right]^{-1}. \quad (27)$$

This procedure enables a more accurate determination of the single-particle energy spectrum and the QP energies by including the effects of electron correlation and dynamic screening, improving upon the HF approximation.

III. MULTIPLE PLASMON POLE APPROXIMATION (MPA)

The multiple plasmon pole approximation (MPA) [17, 18] is an improvement over the single plasmon pole model (PPA) [27, 36–39] used to approximate the dielectric function. Instead of approximating the dielectric function using a single plasmon mode, the MPA assumes the existence of multiple particle-hole collective excitations (they are all called "plasma" for simplicity). The dielectric function is then fitted using these multiple plasma (collective-excitation) modes. The approximation is given by:

$$\epsilon_{\mathbf{QQ}'}^{-1, \text{MPA}}(\tilde{\mathbf{q}}, \nu) - \delta_{\mathbf{QQ}'} = \sum_l^{N_p} \frac{2R_{l, \mathbf{QQ}'}(\tilde{\mathbf{q}})\Omega_{l, \mathbf{QQ}'}(\tilde{\mathbf{q}})}{\nu^2 - \Omega_{l, \mathbf{QQ}'}^2(\tilde{\mathbf{q}})}, \quad (28)$$

where N_p represents the number of plasmon poles, while R and Ω are parameters to be determined. Specifically, $R_{l, \mathbf{QQ}'}(\tilde{\mathbf{q}})$ denotes the residue of the l -th plasmon mode, and $\Omega_{l, \mathbf{QQ}'}(\tilde{\mathbf{q}})$ represents its frequency. To solve for these unknown parameters, we require the values of the dielectric function at $2N_p$ different frequencies.

The advantage of the MPA is that it can simultaneously describe both plasmon modes and the continuous spectrum, avoiding the need for complicated frequency integrations, which greatly speeds up the calculation. Moreover, the accuracy of the approximation can be controlled by adjusting the number of poles in the model, allowing for a balance between computational efficiency and precision. This is especially useful for the spontaneous-symmetry breaking states such as Wigner crystal, where there are multiple collective modes such as acoustic and optical quantum phonons [40].

Supplementary Figure 2 shows some typical examples of the comparison between the numerically calculated inverse dielectric function (dashed lines) and the MPA-fitted inverse dielectric function (solid lines). The red and blue lines correspond to the real and imaginary parts of the inverse dielectric function, respectively. Supplementary Figure 2(a) presents the case of small $\tilde{\mathbf{q}}$ with $\mathbf{G} = 0$ near the Γ point, where a clear plasmon mode is visible near $q = 0$. The MPA approximation accurately captures this plasmon mode and also describes the continuum part of the dielectric function

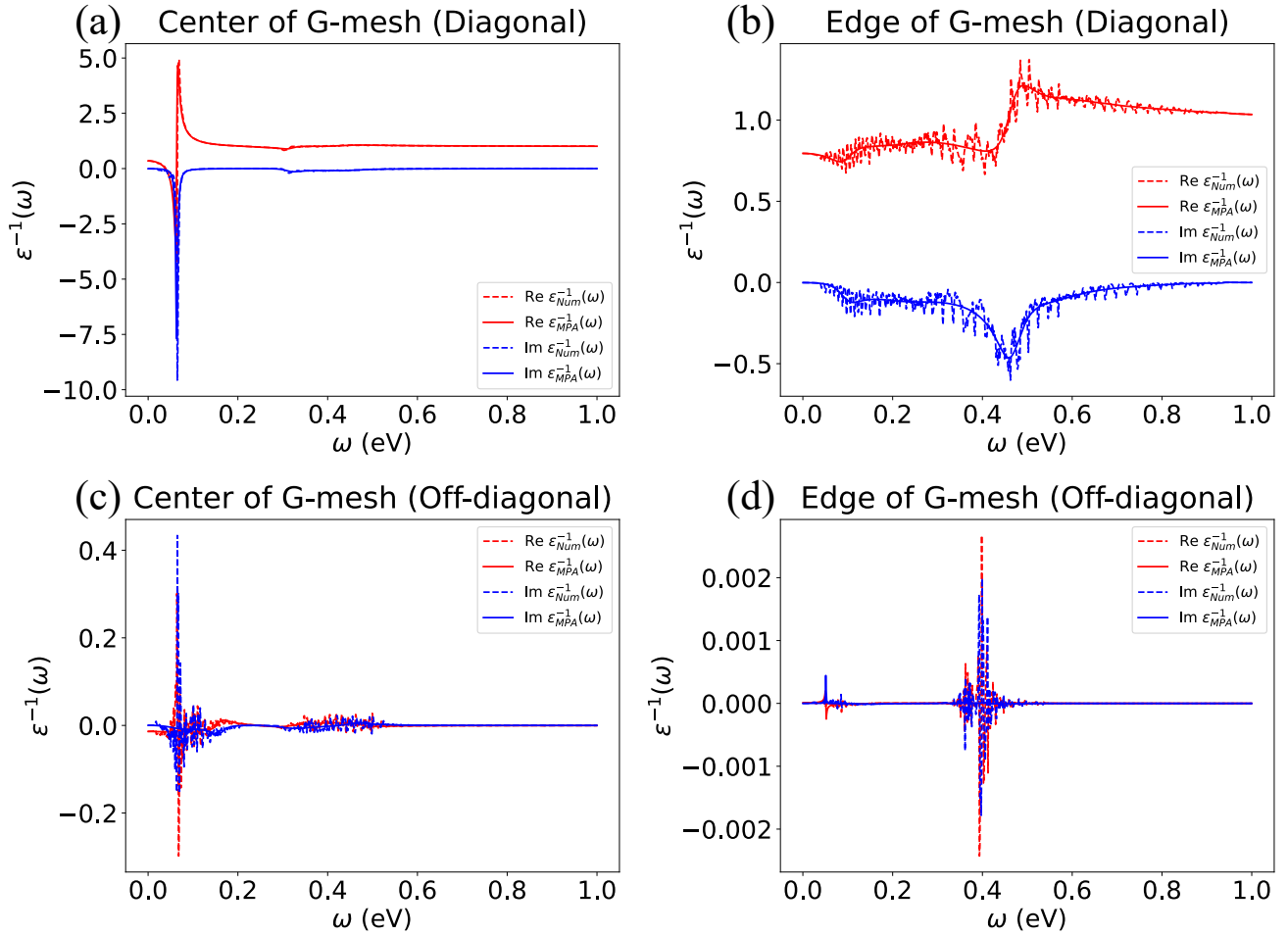


FIG. 2. Comparison between the numerically calculated inverse dielectric function (dashed lines) and the MPA-fitted inverse dielectric function (solid lines). The real part is shown in red, and the imaginary part is shown in blue. (a) Small $\tilde{\mathbf{q}}$ with $\mathbf{G} = 0$ near the Γ point, showing a prominent plasmon mode near $q = 0$. (b) Non-zero \mathbf{G} away from the Γ point, entering the continuum spectrum region. (c) and (d) Off-diagonal elements near and away from the Γ point.

at higher frequencies. In Supplementary Figure 2(b), where $\mathbf{G} \neq 0$ and away from the Γ point, the system enters the continuum spectrum region of the inverse dielectric function. The MPA approximation successfully describes the continuous spectrum using multiple plasmons, a task beyond the capability of the single plasmon pole model. Additionally, the oscillations in the numerically computed inverse dielectric function caused by \mathbf{k} -mesh discretization (or finite-size effects) are smoothed out using MPA. Supplementary Figures 2(c) and 2(d) show the off-diagonal elements of the inverse dielectric function, both near and far from the Γ point. Although these elements are relatively small, the MPA still provides an accurate description.

Using the MPA, we can compute the correlation self-energy more efficiently without losing accuracy. The correlation self-energy Σ_c in the MPA is given by:

$$\Sigma_c(\tilde{\mathbf{k}}, \omega)_{nn} = \frac{1}{N\Omega_0} \sum_{m, \tilde{\mathbf{q}}} \sum_{\mathbf{G}, \mathbf{G}'} \left[\sum_{\lambda, \mathbf{Q}} C_{\lambda \mathbf{G} + \mathbf{Q}, m\tilde{\mathbf{k}} + \tilde{\mathbf{q}}}^* C_{\lambda \mathbf{Q}, n\tilde{\mathbf{k}}} \right]^* \left[\sum_{\lambda', \mathbf{Q}'} C_{\lambda' \mathbf{G}' + \mathbf{Q}', m\tilde{\mathbf{k}} + \tilde{\mathbf{q}}}^* C_{\lambda' \mathbf{Q}', n\tilde{\mathbf{k}}} \right] \times \sum_l^{N_p} \frac{V(\tilde{\mathbf{q}} + \mathbf{G}) R_{\mathbf{G}' \mathbf{G}, l}(\tilde{\mathbf{q}})}{\omega - \varepsilon_{m\tilde{\mathbf{k}} + \tilde{\mathbf{q}}} + i\delta \text{sgn}(\varepsilon_{m\tilde{\mathbf{k}} + \tilde{\mathbf{q}}} - \varepsilon_F) + \Omega_{\mathbf{G}' \mathbf{G}, l}(\tilde{\mathbf{q}})(2f_{m\tilde{\mathbf{k}} + \tilde{\mathbf{q}}} - 1)}, \quad (29)$$

where $f_{m\tilde{\mathbf{k}} + \tilde{\mathbf{q}}}$ represents the Fermi-Dirac distribution function. The derivative of the correlation self-energy with

respect to ω is required to determine the QP weight $Z_{n\tilde{\mathbf{k}}}$:

$$\frac{\partial \Sigma_c(\tilde{\mathbf{k}}, \omega)_{nn}}{\partial \omega} = \frac{-1}{N\Omega_0} \sum_{m, \tilde{\mathbf{q}}} \sum_{\mathbf{G}, \mathbf{G}'} \left[\sum_{\lambda, \mathbf{Q}} C_{\lambda \mathbf{G} + \mathbf{Q}, m\tilde{\mathbf{k}} + \tilde{\mathbf{q}}}^* C_{\lambda \mathbf{Q}, n\tilde{\mathbf{k}}} \right]^* \left[\sum_{\lambda', \mathbf{Q}'} C_{\lambda' \mathbf{G}' + \mathbf{Q}', m\tilde{\mathbf{k}} + \tilde{\mathbf{q}}}^* C_{\lambda' \mathbf{Q}', n\tilde{\mathbf{k}}} \right] \\ \times \sum_l^{N_p} \frac{V(\tilde{\mathbf{q}} + \mathbf{G}) R_{\mathbf{G}' \mathbf{G}, l}(\tilde{\mathbf{q}})}{\left[\omega - \varepsilon_{m\tilde{\mathbf{k}} + \tilde{\mathbf{q}}} + i\delta \text{sgn}(\varepsilon_{m\tilde{\mathbf{k}} + \tilde{\mathbf{q}}} - \varepsilon_F) + \Omega_{\mathbf{G}' \mathbf{G}, l}(\tilde{\mathbf{q}}) (2f_{m\tilde{\mathbf{k}} + \tilde{\mathbf{q}}} - 1) \right]^2}. \quad (30)$$

In the MPA, by fitting the dielectric function using multiple plasma modes, we can more accurately capture the collective excitations of the system, including both collective modes described by poles and the continuum spectra. This approach not only enhances the precision of the calculations but also significantly improves computational efficiency by reducing the complexity of frequency integration.

IV. RANDOM PHASE APPROXIMATION FOR CORRELATION ENERGY

The total energy of the system within RPA framework is given by:

$$E_{\text{tot.}} = E_{\text{kin.}} + E_{\text{HF}} + E_c^{\text{RPA}}, \quad (31)$$

where $E_{\text{kin.}}$ is the kinetic energy, E_{HF} is the HF energy, and E_c^{RPA} represents the correlation energy obtained through the RPA. The inclusion of E_c^{RPA} is crucial, as the HF approximation alone neglects correlation effects, leading to an overestimation of the tendency for symmetry-breaking states such as WC. The RPA provides a more accurate description by incorporating the effects of electron-electron interactions beyond the mean-field level.

The correlation energy in the RPA is given by [19, 20, 25, 26]:

$$E_c^{\text{RPA}} = \frac{1}{4\pi} \int_{-\infty}^{\infty} d\omega \text{Tr} \{ \ln [1 - V\chi^0(i\omega)] + V\chi^0(i\omega) \} \\ = \frac{1}{4\pi} \int_{-\infty}^{\infty} d\omega \sum_{\tilde{\mathbf{q}}, \mathbf{Q}, \mathbf{Q}'} \{ \ln [\delta_{\mathbf{Q}\mathbf{Q}'} - V_{\mathbf{Q}} \delta_{\mathbf{Q}\mathbf{Q}'} \chi_{\mathbf{Q}'\mathbf{Q}}^0(\tilde{\mathbf{q}}, i\omega)] + V_{\mathbf{Q}} \delta_{\mathbf{Q}\mathbf{Q}'} \chi_{\mathbf{Q}'\mathbf{Q}}^0(\tilde{\mathbf{q}}, i\omega) \},$$

where V is the bare Coulomb interaction, and $\chi^0(i\omega)$ calculated by 24 is the non-interacting charge polarizability in the imaginary frequency domain. The first line of the equation presents a general expression for the RPA correlation energy in matrix form, involving a trace over all possible interaction channels. The second line expands this expression into the momentum space, where $\tilde{\mathbf{q}}$ and \mathbf{Q} denote momentum vectors, and $\chi_{\mathbf{Q}'\mathbf{Q}}^0(\tilde{\mathbf{q}}, i\omega)$ are the matrix elements of the non-interacting susceptibility.

By combining the GW approximation and the RPA, we achieve a more comprehensive description of the total energy. The GW approximation improves the single-particle energy spectrum, leading to more accurate values for $\chi^0(i\omega)$, while the RPA incorporates the dynamic charge fluctuation effects to provide a more reliable estimate of the correlation energy. This approach is essential for capturing the delicate balance between the FL state and other competing spontaneous symmetry-breaking phases, such as the WC state, especially in low-carrier-density interacting two-dimensional systems.

V. DATA FITTING FOR CRITICAL WIGNER-SEITZ RADIUS r_s^* IN 2DEG

To determine the critical Wigner-Seitz radius r_s^* for the transition between the FL state and the WC state in 2DEG system, we perform a detailed data fitting analysis. The total energies of both the WC and FL states are calculated using the GW +RPA framework, which incorporates both the exchange and correlation effects more accurately compared to the HF approximation.

The energy of the Wigner crystal state E_{WC} is fitted using the following expression [5]:

$$E_{\text{WC}} = \frac{c_1}{r_s} + \frac{c_{3/2}}{r_s^{3/2}} + \frac{c_2}{r_s^2} + \frac{c_{5/2}}{r_s^{5/2}} + \frac{c_3}{r_s^3}, \quad (32)$$

where the coefficients $c_1, c_{3/2}, c_2, c_{5/2}$, and c_3 are fitting parameters that capture the behavior of the WC state as a function of the Wigner-Seitz radius r_s . These terms account for various contributions to the energy, including kinetic,

exchange, and correlation energies. The form of this equation ensures a smooth interpolation of the energy in the WC state regime.

For the Fermi liquid state, the total energy E_{FL} is composed of two parts: the Hartree-Fock energy $E_{\text{FL}}^{\text{HF}}$ and the correlation energy E_{FL}^c [12]:

$$E_{\text{FL}} = E_{\text{FL}}^{\text{HF}} + E_{\text{FL}}^c. \quad (33)$$

The Hartree-Fock energy for the FL state is given by:

$$E_{\text{FL}}^{\text{HF}} = \frac{1}{2r_s^2} - \frac{4\sqrt{2}}{3\pi r_s}, \quad (34)$$

where the first term represents the kinetic energy contribution, and the second term accounts for the exchange energy in the FL state. However, the Hartree-Fock approximation alone does not include correlation effects, which are crucial for accurately capturing the properties of the FL state.

To include the correlation effects, we use an empirical formula for the correlation energy E_{FL}^c :

$$E_{\text{FL}}^c = a_0 \left\{ 1 + Ax^2 \left[B \ln \frac{x+a_1}{x} + C \ln \frac{\sqrt{x^2 + 2a_2x + a_3}}{x} + D \left(\arctan \frac{x+a_2}{\sqrt{a_3 - a_2^2}} - \frac{\pi}{2} \right) \right] \right\}, \quad (35)$$

where $x = \sqrt{r_s}$. The parameters a_0 , a_1 , a_2 , and a_3 are fitting parameters that are determined through numerical fitting to the GW +RPA data. The coefficients A , B , C , and D are given by:

$$A = \frac{2(a_1 + 2a_2)}{2a_1a_2 - a_3 - a_1^2}, \quad (36)$$

$$B = \frac{1}{a_1} - \frac{1}{a_1 + 2a_2}, \quad (37)$$

$$C = \frac{a_1 - 2a_2}{a_3} + \frac{1}{a_1 + 2a_2}, \quad (38)$$

$$D = \frac{F - a_2C}{\sqrt{a_3 - a_2^2}}, \quad (39)$$

$$F = 1 + (2a_2 - a_1) \left(\frac{1}{a_1 + 2a_2} - \frac{2a_2}{a_3} \right). \quad (40)$$

These expressions are derived to provide an accurate representation of the correlation energy in the FL state, taking into account the complex interaction effects in the 2DEG. The GW +RPA method gives a more precise calculation of χ^0 , leading to a reliable estimation of the correlation energy.

By fitting the total energies E_{WC} and E_{FL} obtained from the GW +RPA calculations, we identify the critical Wigner-Seitz radius r_s^* where the energies of the WC and FL states intersect. This intersection marks the transition point between the gapless Fermi liquid state and the charge-gapped Wigner crystal state. In our calculations for the conventional 2DEG system, this critical value is found to be $r_s^* \sim 19.2$, significantly improving upon the values obtained from the HF or HF+RPA calculations. This refined critical radius demonstrates the importance of accurately including correlation effects through the GW +RPA framework when studying phase transitions in interacting electron systems.

VI. MORE RESULTS ABOUT n -ORDER DIRAC FERMION MODELS FOR $n=2, 3, 4, 5$, AND 6

HF results

Supplementary Figure 3 shows the HF results for the WC condensation energy as a function of lattice constant L_s for n -order Dirac fermion models with $n = 2$ to 6. For $n = 2$ to 6 layers (corresponding to Supplementary

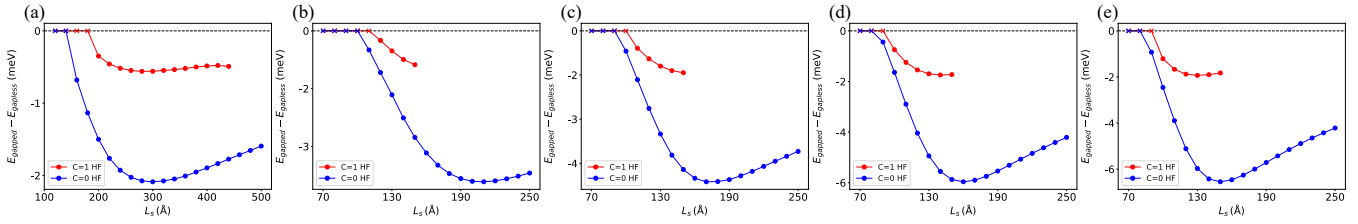


FIG. 3. (a)-(e) The HF results for the WC condensation energy as a function of lattice constant L_s for n -order Dirac fermion models with $n = 2$ to 6 , respectively.

Figures 3(a)-(e)), the HF ground states for all cases are the Chern-number-0 WC states. Additionally, there exists a metastable Chern-number-1 WC state at certain values of L_s for each case. As the number of layers increases, the condensation energies of both types of WC states at the same L_s would increase in amplitude, indicating that the WC states become more stable with higher layer numbers within HF framework. This is due to the fact that systems with more layers exhibit higher density of states near Fermi energy, which further enhances interaction effects and stabilizes the WC states.

It is worth noting that the Berry curvature of the non-interacting conduction band of the n -order Dirac-fermion model can be calculated analytically as follows:

$$\Omega(\mathbf{k}, n) = \frac{\gamma^2 n^2 \Delta k^{2n-2}}{2(\gamma^2 k^{2n} + \Delta^2)^{3/2}}, \quad (41)$$

where $\gamma = (-1/t_{\perp})^{n-1} v_F^n$. The Berry curvature $\Omega(\mathbf{k}, n)$ is peaked at the wavevector k_{peak} :

$$k_{\text{peak}} = \frac{1}{v_F} \left(\frac{n-1}{n+2} \right)^{\frac{1}{2n}} \Delta^{\frac{1}{n}} t_{\perp}^{\frac{n-1}{n}}. \quad (42)$$

As the number of layers increases, k_{peak} shifts toward larger value. Actually, our HF calculations indicate that whenever the Fermi wavevector k_F coincides with k_{peak} , the system would undergo WC transition with the critical WC lattice constant L_s^* , and the distance between Γ_s and K_s in the corresponding first Brillouin zone given by $4\pi/(3L_s^*) \sim k_F \sim k_{\text{peak}}$. In other words, WC state would emerge at larger carrier density with larger n under HF approximation. Using 42, and assuming that $4\pi/(3L_s^*) = k_{\text{peak}}$, we obtain the following expression for the critical L_s^* :

$$L_s^* = \frac{4\pi}{3k_{\text{peak}}} = \frac{4\pi}{\frac{3}{v_F} \left(\frac{n-1}{n+2} \right)^{\frac{1}{2n}} \Delta^{\frac{1}{n}} t_{\perp}^{\frac{n-1}{n}}}. \quad (43)$$

Supplementary Figure 4 shows the variation of L_s^* (at the WC transition onsets) as a function of the layer number

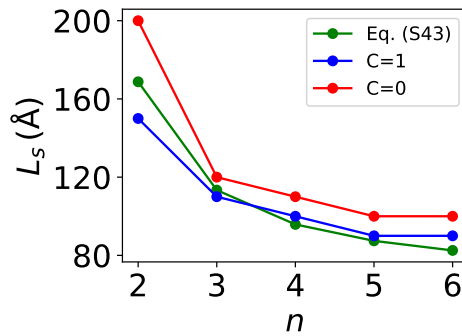


FIG. 4. L_s^* at which the WC transition onsets as a function of the layer number n . The Green circles represent the values calculated using Eq. (43). The blue and red solid circles denote the values obtained from actual numerical calculations, as presented in Supplementary Figure 3.

n . It can be seen that the L_s^* estimated using Eq. (43) closely matches the actual results extracted from numerical calculations (presented in Supplementary Figure 3).

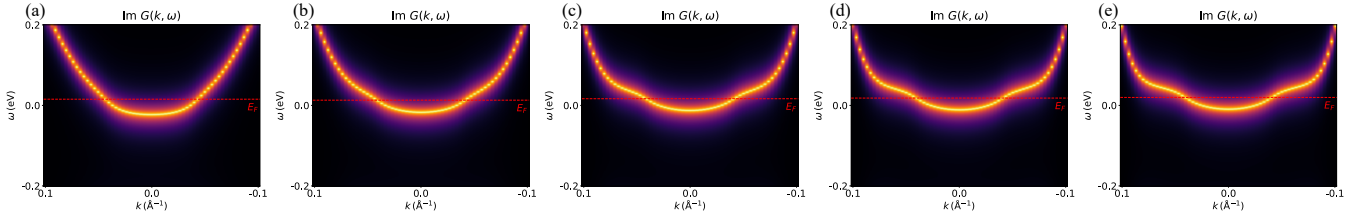


FIG. 5. (a)-(e) The HF single-particle energy spectra of the FL state for n -order Dirac fermion models with $n = 2$ to 6 at $L_s = 150 \text{ \AA}$, respectively. The red dashed lines mark the Fermi energies.

Supplementary Figures 5(a)-(e) show the HF single-particle energy spectra of the FL state at for n -order Dirac fermion models with $n = 2$ to 6 at $L_s = 150 \text{ \AA}$, respectively. As the number of layers increases from $n = 2$ to $n = 6$, the low-energy bands become increasingly less dispersive, indicating stronger correlation effects with higher n . For lower n , such as in Supplementary Figure 5(a) and (b), the bands near the Fermi surface retain a relatively more dispersive character. However, as seen in Supplementary Figure 5(c)-(e), the bands flatten further, showing the enhanced influence of electron-electron interactions as the layer number increases.

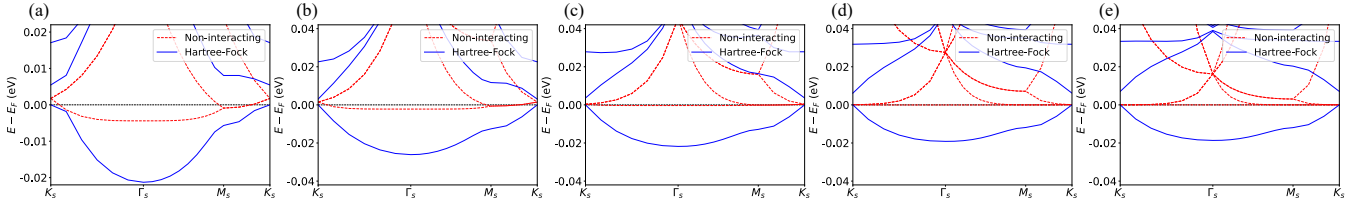


FIG. 6. (a)-(e) The HF band structures for the Chern-number-1 WC state for n -order Dirac fermion models with $n = 2$ at $L_s = 200 \text{ \AA}$ and $n = 3$ to 6 at $L_s = 150 \text{ \AA}$, respectively. The gray dashed lines mark the Fermi energies.

Supplementary Figures 6(a)-(e) present the HF band structures for the Chern-number-1 WC state for n -order Dirac fermion models with $n = 2$ at $L_s = 200 \text{ \AA}$ and $n = 3$ to 6 at $L_s = 150 \text{ \AA}$, respectively. For $n = 2$, the system converges to the Chern-number-0 state from the same initial conditions (indicating that the Chern-number-1 state is unstable at $L_s = 150 \text{ \AA}$ for $n = 2$). The red dashed lines indicate the non-interacting results, where it can be observed that as n increases, the low-energy bands become significantly flatter. The blue solid lines show the HF results, where an increase in n leads to a gradual reduction in the bandwidth and a corresponding increase in the band gap of the WC states. These trends highlight the enhanced impact of electron-electron interactions on the band structure with increasing layer number, particularly in stabilizing the Chern-number-1 state.

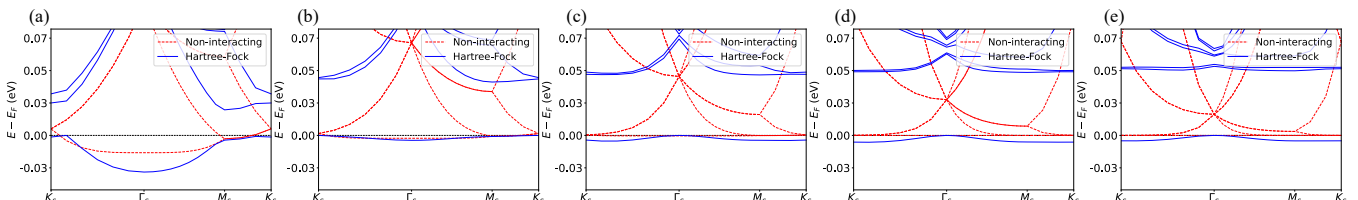


FIG. 7. (a)-(e) The HF band structures for the Chern-number-0 WC state for n -order Dirac fermion models with $n = 2$ to 6 at $L_s = 150 \text{ \AA}$, respectively.

Supplementary Figures 7(a)-(e) display the HF band structures for the Chern-number-0 WC state for n -order Dirac fermion models with $n = 2$ to 6 at $L_s = 150 \text{ \AA}$, respectively, in comparison with the Chern-number-1 bands shown in Supplementary Figure 6. As n increases, a key difference emerges: the low-energy bands in the Chern-number-0 state are more flat compared to those in the Chern-number-1 state, indicating a relatively stronger interaction-induced renormalization. In contrast to the Chern-number-1 state, the bandwidth of the Chern-number-0 state does not increase significantly due to interactions. This indicates a stronger tendency for electron localization in the Chern-number-0 state. This observation is consistent with the real-space charge distribution discussed in the main text, where electrons in the Chern-number-0 state form a more localized charge pattern.

HF+RPA and GW+RPA Results

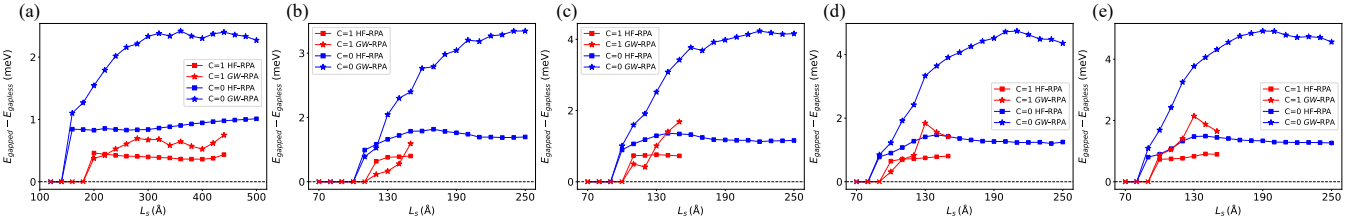


FIG. 8. (a)-(e) The HF+RPA and *GW*+RPA results for the WC condensation energy as a function of lattice constant L_s for n -order Dirac fermion models with $n = 2$ to 6 , respectively.

Compared to the HF ground-state results in Supplementary Figure 3, the inclusion of RPA correlation energy indicates that neither type of WC state remains as the ground state, as shown in Supplementary Figure 8. Additionally, the Chern-number-0 WC state becomes even less stable than the Chern-number-1 WC state. The more accurate *GW*+RPA approach further enhances the effect of RPA correlation energy, making the WC states even more unfavorable. As the layer number n increases, the WC states become increasingly unstable, indicating that correlation energy plays a critical role in destabilizing the WC states. This outcome is in direct contrast to the pure HF approximation, which predicts the WC state as the ground state. These results highlight that while HF tends to overestimate the stability of the WC state, the inclusion of correlation effects through HF+RPA and *GW*+RPA provides a more comprehensive understanding of the ground state in these Dirac-fermion systems.

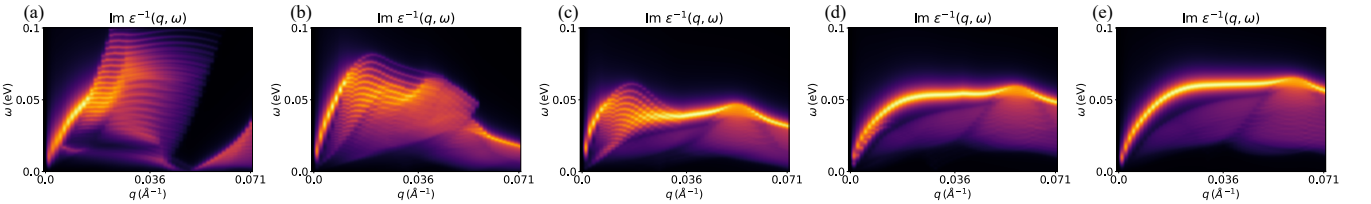


FIG. 9. (a)-(e) The electron excitation spectra calculated based on the HF band for the Chern-number-0 WC state for n -order Dirac fermion models with $n = 2$ to 6 at $L_s = 150$ Å, respectively.

Supplementary Figures 9(a)-(e) show the collective excitation spectra for n -order Dirac fermion models with $n = 2$ to 6 at $L_s = 150$ Å, respectively, calculated based on the HF energy bands. Here we focus on the most significant intraband low-energy collective excitations. Besides the particle-hole continuum, in the limit where q approaches 0, all layers display the typical \sqrt{q} dependence, indicating the presence of a gapless plasmon mode. However, the bandwidth of these modes differs notably in the $n = 2, 3, 4$ systems. As the layer number increases to $n = 5$ and $n = 6$, the HF bands become extremely flat, and the collective excitation spectra exhibit a nearly momentum-independent branch over a certain range of wavevector. This behavior implies the presence of a prominent satellite feature in the *GW* single-particle excitation spectra.

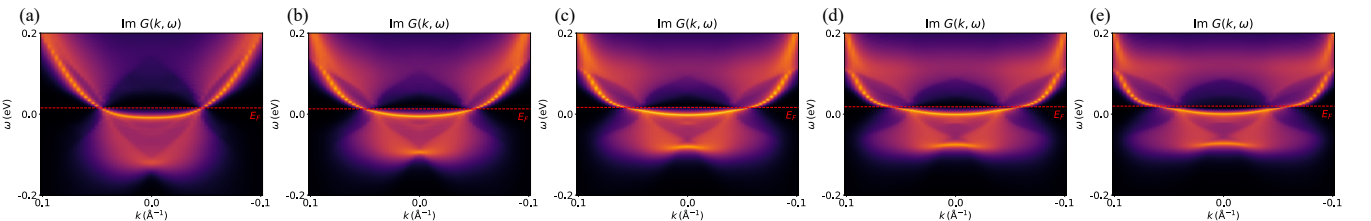


FIG. 10. (a)-(e) The *GW*-calculated single-particle energy spectra for the FL state for n -order Dirac fermion models with $n = 2$ to 6 at $L_s = 150$ Å, respectively.

Supplementary Figures 10(a)-(e) show the *GW*-calculated single-particle energy spectra for the FL state for n -order Dirac fermion models with $n = 2$ to 6 at $L_s = 150$ Å, respectively. Near the Fermi surface, distinct plasmon satellites are visible, indicating the influence of electron-plasmon interactions. Furthermore, as shown in Supplementary

Figure 9, with increasing layer number, a progressively flatter and nearly momentum-independent spectral feature emerges below the Fermi surface. This flat feature arises from the interaction between electrons and plasmons, leading to the formation of plasmarons or plasma-polarons. Similar features in the single-particle spectra due to electron-plasmon couplings have also been reported in carrier-doped monolayer graphene [30–32]. The appearance of this feature becomes more pronounced with smaller bandwidth in higher-layer systems, resulting from the flatter bands in the corresponding non-interacting models.

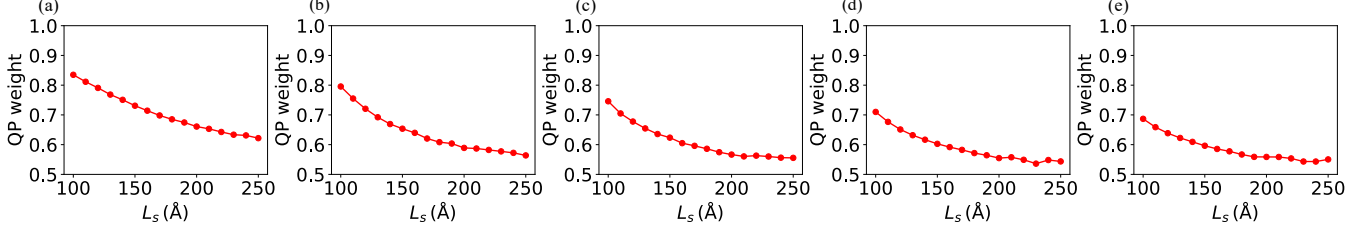


FIG. 11. (a)-(e) The GW -calculated QP weight for the FL state for n -order Dirac fermion models with $n = 2$ to 6 at $L_s = 150 \text{ \AA}$, respectively.

Supplementary Figures 11(a)-(e) show the GW -calculated QP weight for the FL state for n -order Dirac fermion models with $n = 2$ to 6 at $L_s = 150 \text{ \AA}$, respectively. As the layer number n increases, the QP weight at the same L_s gradually decreases, indicating a reduction in the coherent part of the spectral weight. This reduction reflects the increasing interaction effects in higher-layer systems, consistent with the enhanced electron-plasmon interactions observed in the corresponding GW single-particle spectra.

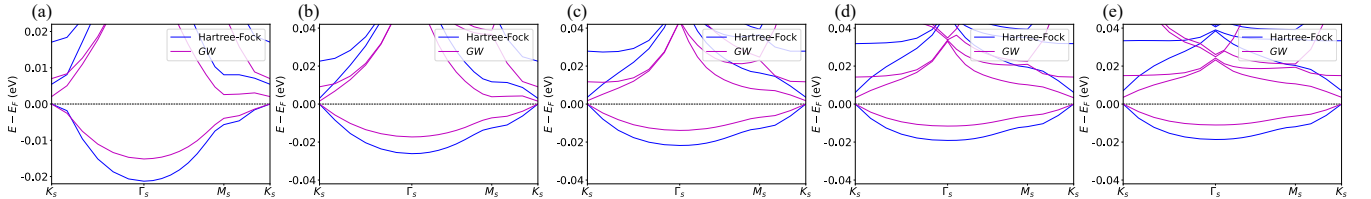


FIG. 12. (a)-(e) The GW -calculated single-particle energy spectra for the Chern-number-1 WC state for n -order Dirac fermion models with $n = 2$ at $L_s = 200 \text{ \AA}$ and $n = 3$ to 6 at $L_s = 150 \text{ \AA}$, respectively.

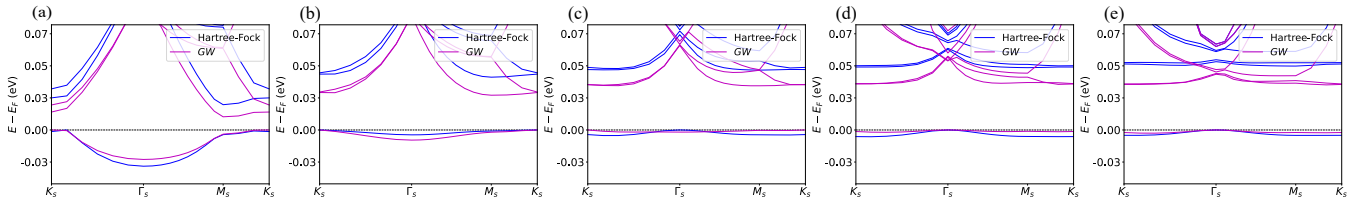


FIG. 13. (a)-(e) The GW -calculated single-particle energy spectra for the Chern-number-0 WC state for n -order Dirac fermion models with $n = 2$ to 6 at $L_s = 150 \text{ \AA}$, respectively.

Supplementary Figures 12(a)-(e) and Supplementary Figures 13(a)-(e) show the GW quasi-particle band structures for the Chern-number-1 and Chern-number-0 WC states for n -order Dirac fermion models with $n = 2$ to 6 at $L_s = 150 \text{ \AA}$ (except for Chern-number-1 band with $n = 2$ replaced to that at $L_s = 200 \text{ \AA}$ due to its instability at $L_s = 150 \text{ \AA}$), respectively, compared to the HF results in Supplementary Figures 6(a)-(e) and Supplementary Figures 7(a)-(e). The GW correction introduces dynamical screening of the Coulomb interactions, resulting in a more accurate calculation of the bandwidth and band gap. This correction mitigates the overestimation by the HF approximation, leading to a reduced bandwidth and a more realistic depiction of the gap.

Summary

In this section, we have presented a comprehensive analysis of n -order Dirac fermion models for $n = 2$ to 6, exploring both the HF, and more advanced HF(GW)+RPA calculations. The HF results indicate that with increasing layer number, the WC states become more stable due to enhanced electron-electron interactions. However, the inclusion of RPA correlation energy in the HF(GW)+RPA framework reveals that neither the Chern-number-0 nor the Chern-number-1 WC states remain as the ground state, highlighting the crucial role of correlation effects in destabilizing these states.
